Communication

Ethylammonium Bromide- and Potassium-Added CH₃NH₃PbI₃ Perovskite Solar Cells

Shuhei Terada [1], Takeo Oku [1,*], Atsushi Suzuki [1], Masanobu Okita [2], Sakiko Fukunishi [2], Tomoharu Tachikawa [2] and Tomoya Hasegawa [2]

[1] Department of Materials Science, The University of Shiga Prefecture, 2500 Hassaka, Hikone 522-8533, Japan
[2] Osaka Gas Chemicals Company, Limited, 5-11-61 Torishima, Konohana-ku, Osaka 554-0051, Japan
[*] Correspondence: oku@mat.usp.ac.jp; Tel.: +81-749-28-8368

Abstract: Perovskite solutions with added potassium iodide (KI) and ethylammonium bromide (EABr) were used to fabricate perovskite solar cells in ordinary air at 190 °C. The addition of EABr and KI induced (100)-oriented perovskite crystals, which resulted in the improvement in short-circuit current densities and conversion efficiencies. The short-circuit current density, open circuit voltage, and conversion efficiency of the best device were 21.0 mA cm^{-2}, 0.942 V, and 12.88%, respectively. First-principles calculations also indicated a decrease in total energy per cell and an increase in energy gaps, which agreed with the improved results of device stabilities and photovoltaic properties.

Keywords: perovskite; solar cells; ethylammonium; potassium

1. Introduction

Although silicon solar cells are widely used in the world, greater cost reduction and development of usability are needed for future solar cell devices. Perovskite solar cells are one of the alternate candidates for future photovoltaic devices [1–4], and the progress is quite fast-paced [5–7]. However, the perovskite layer tends to deteriorate due to various factors such as crystal structures [8], and long-term stability is one of the most serious problems [9–11]. It has also been reported that the stability is improved by substituting a part of methylammonium (CH₃NH₃, MA) in the perovskite crystal with the alkali metals such as cesium (Cs) and rubidium (Rb) [12–14]. The performance of perovskite solar cells can also be improved by adjusting the doping amount of potassium (K) [15,16], which is cheaper than Cs and Rb. K has been reported to reduce defects [16,17] and improve stability by entering the defects of the MA site [18–20]. The stabilities were also reported to be improved by using ethylammonium (CH₃CH₂NH₃, EA), which is more stable than MA [21,22]. There have been few reports on the effects of co-addition of ethylammonium bromide and potassium on the photovoltaic properties and microstructures.

The purpose of the present work was to fabricate and characterize perovskite solar cells in which ethylammonium bromide (EABr) and potassium iodide (KI) were added to standard MAPbI₃. Polysilane was also used for a hole transport and protecting layer for perovskite compounds. From the viewpoint of the commercialization of the perovskite solar cells, the fabrication procedures should be under ordinary air. The effects of EABr and KI co-addition to perovskite crystals on their photovoltaic properties were investigated using light-induced current density–voltage (*J-V*) measurements, external quantum efficiency (EQE), optical microscopy (OM), X-ray diffraction (XRD), and first-principles calculations.

2. Materials and Methods

All processes to fabricate photovoltaic cells were performed in air [23,24], as shown in Figure 1. F-doped tin oxide (FTO) substrates were cleaned in an ultrasonic bath with acetone and methanol and dried under nitrogen gas. The FTO substrates were treated with an ultraviolet ozone cleaner (ASM401N, Asumi Giken, Tokyo, Japan) for 15 min.

TiO$_x$ precursor solutions (0.15 and 0.30 M) were prepared from titanium diisopropoxide bis(acetyl acetonate) (Sigma Aldrich, Tokyo, Japan) and 1-butanol (FUJIFILM Wako Pure Chemical Corporation, Osaka, Japan). Both TiO$_x$ precursor solutions were spin-coated onto the FTO substrate at 3000 rpm for 30 s and annealed at 125 °C for 5 min, and the 0.30 M precursor was spin-coated twice to form a uniform layer. After that, the FTO substrate was annealed at 550 °C for 30 min to form a compact TiO$_2$ layer. A mesoporous TiO$_2$ precursor solution was spin-coated onto the compact TiO$_2$ layer at 5000 rpm for 30 s using TiO$_2$ paste. The TiO$_2$ paste was prepared using TiO$_2$ powder (P-25, Aerosil, Tokyo, Japan, 200 mg) and poly(ethylene glycol) (PEG, Nacalai Tesque, Kyoto, Japan, #20000, 20 mg) in distilled water (0.5 mL). This solution was mixed with acetylacetone (FUJIFILM Wako Pure Chemical Corporation, 20 μL) and the Triton X-100 surfactant (Sigma Aldrich, 10 μL) for 30 min and was then allowed to stand for 24 h to suppress bubble formation in the solution. The FTO substrates with the TiO$_2$ were annealed at 550 °C for 30 min to form mesoporous TiO$_2$ layers.
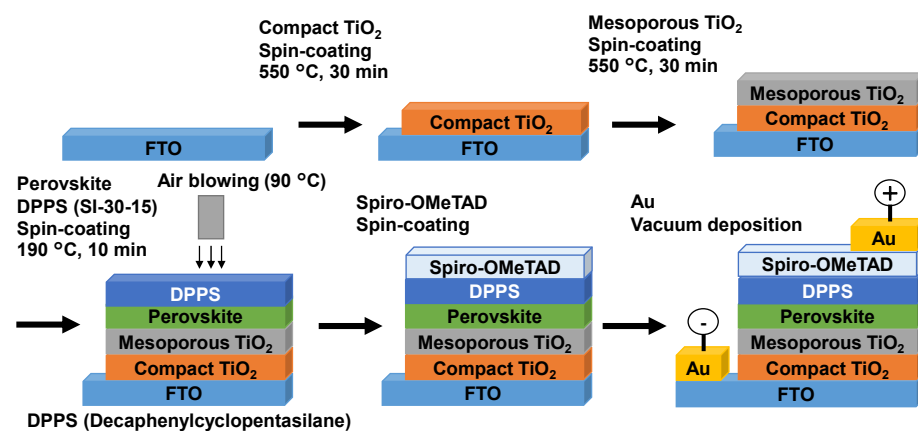
Figure 1. Schematic illustration for the fabrication process of the present photovoltaic cells.

The perovskite compounds were prepared by mixing N,N-dimethylformamide (DMF; Sigma Aldrich) solutions of CH$_3$NH$_3$I (Tokyo Chemical Industry, Tokyo, Japan), CH$_3$CH$_2$NH$_3$Br (Tokyo Chemical Industry), PbCl$_2$ (Sigma Aldrich), and KI (FUJIFILM Wako Pure Chemical Corporation) at 60 °C [14,18]. Standard MAPbI$_3$ precursors with molar concentrations of MAI and PbCl$_2$ of 2.4 and 0.8 M, respectively, were prepared [25,26], and MA$_{0.95−x}$EA$_x$K$_{0.05}$PbI$_{3−3x}$Br$_{3x}$ (x = 0.1, 0.2, 0.3, 0.4, or 0.5) precursors were also prepared. Solutions containing the perovskite precursors were spin-coated onto the mesoporous TiO$_2$ layers at 2000 rpm for 60 s using the hot air-blowing method [8,27]. Polysilane (decaphenyl-cyclopentasilane, DPPS, OGSOL SI-30-15, Osaka Gas Chemical, Osaka, Japan) was dropped during spin-coating [28–31]. The temperature of the FTO substrates during hot air-blowing was measured at 90 °C. The cells were then annealed at 190 °C for 10 min in ambient air. The temperature and humidity of the air atmosphere during device fabrication were ~21 °C and ~23%, respectively.

A hole transport layer (HTL) was formed by spin-coating at 4000 rpm for 30 s. The HTL precursor solution was prepared by adding 2,2′,7,7′-tetrakis(N,N-di-p-methoxyphenylamine)-9,9′-spirobifluorene (spiro-OMeTAD, Sigma Aldrich, 36.1 mg) to chlorobenzene (0.5 mL; FUJIFILM Wako Pure Chemical Corporation) and stirring the solution for 24 h. A solution of lithium bis(trifluoromethylsulfonyl) imide (Li-TFSI, Tokyo Chemical Industry, 260 mg) in acetonitrile (Nacalai Tesque, 0.5 mL) was also prepared by stirring for 24 h. The former spiro-OMeTAD solution with 4-tert-butylpyridine (Sigma Aldrich, 14.4 μL) was mixed with the latter Li-TFSI solution (8.8 μL) for 30 min at 70 °C and cooled to ambient temperature. Finally, a gold (Au) top electrode was formed by vacuum evaporation. Film thicknesses of compact TiO$_2$, mesoporous TiO$_2$/perovskite, DPPS, spiro-OMeTAD, and Au were about 50 nm, 600 nm, 10 nm, 50 nm, and 200 nm, respectively, for the present process [32,33].

The *J-V* characteristics (B2901A, Keysight, Santa Rosa, CA, USA) of the photovoltaic cells were measured when illuminated with a solar simulator (XES-301S, San-ei Electric, Osaka, Japan) at 100 mW cm^{-2} with a 1.5 air mass. The solar cells were illuminated through the side of the FTO substrates, and the exposed area was 0.080 cm^2. The EQEs of the solar cells were also measured using an incident photon-to-electron conversion efficiency measurement system (QE-R, Enli Technology, Kaohsiung, Taiwan). The microstructures of the perovskite layers were investigated with an X-ray diffractometer (D2 PHASER, Bruker, Billerica, MA, USA), while the surface morphologies of the perovskite layers were examined using an optical microscope (Eclipse E600, Nikon, Tokyo, Japan).

3. Results and Discussion

The *J-V* characteristics of photovoltaic devices containing K and EA are shown in Figure 2a. The photovoltaic parameters are summarized in Table 1, where J_{SC} was the short-circuit current density, V_{OC} was the open-circuit voltage, FF was the fill factor, R_s was the series resistance, R_{sh} was the shunt resistance, η was the conversion efficiency, and η_{ave} was the average efficiency of three cells. The device with a standard MAPbI$_3$ perovskite had an η of 9.33%, while devices with K- and EA-doped perovskites had increased efficiencies with the addition of 30% EABr and decreased efficiencies for EABr additions above 40%. The highest η (12.88%) was obtained for the device with MA$_{0.65}$EA$_{0.30}$K$_{0.05}$PbI$_{2.1}$Br$_{0.9}$ perovskite. Although J_{SC} values of devices with K- and EA-doped perovskites were lower than those of the standard device, their V_{OC} values were higher, which was due to the Br content as described in the EQE data. J_{SC} values increased over the range of 10% to 30% of added EABr, and the reason will be described later for the microstructure model of the perovskite. FF values of the device are generally large with an increased area under the *J-V* curve. The FF is related to the degree of "bending" of the *J-V* curve, and a higher degree of bending means a higher FF value. Since the *J-V* curve of EABr 30% has a lower degree of bending, the FF of EABr 30% is less than that of EABr 20%. The devices with only 5% KI-doped perovskite or 20% EABr-doped perovskite had been investigated in previous studies [20,22], and conversion efficiencies of 0.72% and 8.65% were obtained, respectively. Since these efficiencies were not so high, these compositions were not shown in the present work.
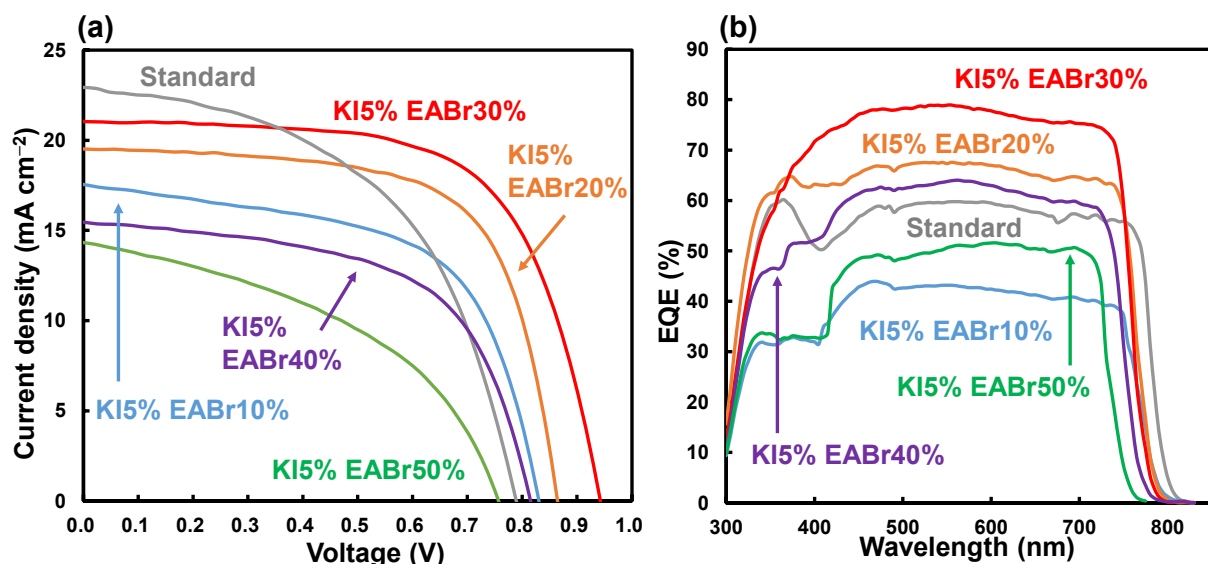

Figure 2. (**a**) *J-V* characteristics and (**b**) EQE of perovskite solar cells that contained KI- and EABr-doped perovskite.

Table 1. Measured photovoltaic parameters of the present perovskite solar cells.

Device		J_{SC} (mA cm^{-2})	V_{OC} (V)	FF	R_S (Ω cm^2)	R_{Sh} (Ω cm^2)	η (%)	η_{ave} (%)	HI	E_g (eV)	t
KI (%)	EABr (%)										
0	0	22.9	0.789	0.516	7.29	277	9.33	8.11	0.014	1.556	0.912
5	10	17.5	0.830	0.593	5.52	249	8.63	6.76	0.084	1.565	0.919
5	20	19.5	0.864	0.665	4.24	1015	11.22	9.46	0.073	1.582	0.933
5	30	21.0	0.942	0.649	5.69	2209	12.88	11.11	0.076	1.600	0.947
5	40	15.5	0.815	0.586	6.14	437	7.38	6.04	0.063	1.613	0.961
5	50	14.3	0.757	0.440	9.99	163	4.77	3.25	0.187	1.640	0.975

The hysteresis index (HI) values were also calculated from the *J-V* data with different scan directions and listed in Table 1. The HI values were estimated from the following equation [34]: HI = $(J_{RH} - J_{FH})/J_{RH}$, where J_{RH} is the current density at the half open-circuit voltage for the reverse scan and J_{FH} is the current density at the half open-circuit voltage for the forward scan. When there is no hysteresis, the HI is equal to 0. The HI values of KI- and EABr-added devices were a little higher than that of the standard device.

To estimate the structural stability of perovskite compounds, a tolerance factor (*t*) is used [8,35,36] with the following equation: $t = \frac{r_A + r_X}{\sqrt{2}(r_B + r_X)}$, where r_A, r_B, and r_X are the ionic radii of the A, B, and X ions for ABX$_3$ perovskite structures, respectively [8]. When the *t*-value is 1, the perovskite compound has a stable crystal structure with cubic symmetry. From the previous experimental studies on perovskite compounds, the perovskite structure could be formed in the range of $0.813 \leq t \leq 1.107$. Calculated *t*-factors of perovskite compounds are listed in Table 1. From this calculation, it is shown that co-addition of EABr and KI could be an effective way to stabilize the MAPbI$_3$ structure.

The EQE vs. wavelength of the photovoltaic devices is shown in Figure 2b. The estimated energy gaps, calculated via linear fits with band gap calculator software (Enlitech), are summarized in Table 1. The energy gap (E_g) increased with the addition of K and EA. The EQEs of devices containing 20% and 30% EABr-doped perovskites were higher than those for the standard device, and the added EABr increased J_{SC}, as noted above. The addition of Br increased V_{OC} because of the increase in E_g, like CH$_3$NH$_3$PbBr$_3$ with an E_g of 2.3 eV [37], and the addition of EA suppressed decreases in J_{SC}. The EQE values of devices are low at a wavelength between 350 and 400 nm, which might be due to the optical absorption by TiO$_2$. The quality of TiO$_2$ should be improved further. A J_{SC} value of the standard device calculated from the EQE was lower than that obtained from *J-V* data, which might be related to sensitivity to the light intensity.

Optical microscopy images of the perovskite layers on the devices are shown in Figure 3a. The device with 30% EABr exhibited the most uniform, homogenous film morphology. Non-uniform films were formed with 40% or 50% EABr.

XRD patterns of the photovoltaic devices are shown in Figure 3b. The (100) peak intensity in the device with 30% EABr was the highest. In Table 2, the measured lattice constants of the perovskite compounds indicated that the unit cell volumes decreased with the addition of KI and EABr relative to that of standard MAPbI$_3$.

The crystal orientation of the perovskite grains was estimated from the ratios of the (100) intensity (I_{100}) of the perovskite to the (210) intensity (I_{210}) of the perovskite, as listed in Table 2. When the crystal planes in the perovskite crystallites were randomly aligned, the ratio I_{100}/I_{210} was 2.08 [8]. For the standard device, I_{100}/I_{210} was 2.4, which indicated that the (100) planes were randomly aligned. I_{100}/I_{210} was 20.0 for the devices with 30% EABr, which indicated that the (100) planes of the perovskite crystals were highly aligned with respect to the FTO substrate.
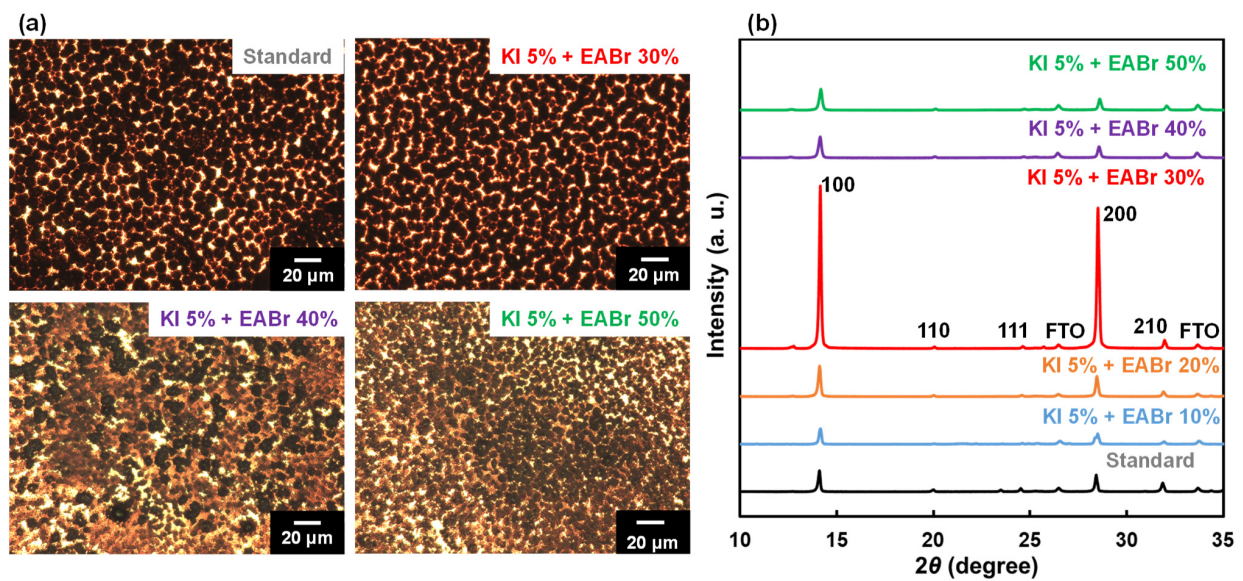
Figure 3. (**a**) Optical microscope images of perovskite solar cells. (**b**) X-ray diffraction patterns of the perovskite solar cells.

Table 2. Structural parameters of perovskite crystals with added KI and EABr.

| Device		Lattice Constant (Å)	Crystallite Size (Å)	Orientation I_{100}/I_{210}
KI (%)	EABr (%)			
0	0	6.279(1)	868	2.4
5	10	6.274(0)	596	5.9
5	20	6.263(2)	663	6.4
5	30	6.253(3)	1019	20.0
5	40	6.247(3)	640	2.2
5	50	6.233(1)	532	1.9

Figure 4a shows a comparison of the crystal orientations and J_{SC} values as a function of EA concentration. There was a correlation between J_{SC} and the crystal orientation, and the improved crystal orientation increased J_{SC} and led to decreased R_S.
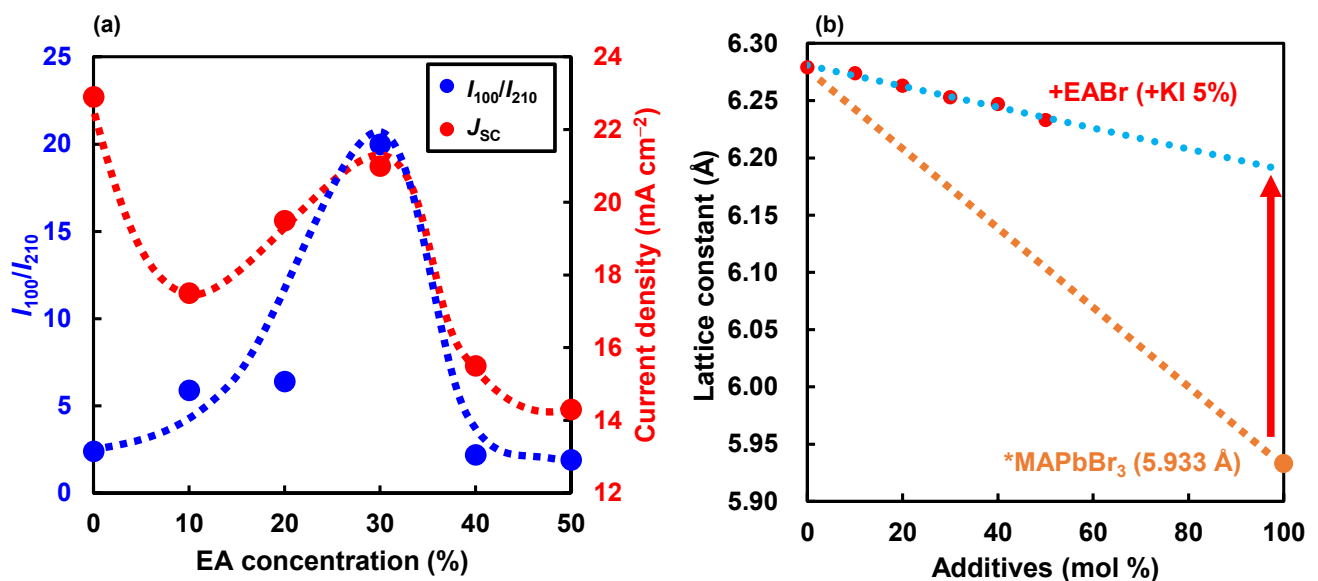
Figure 4. (**a**) Changes in the (100) orientation and short-circuit current densities, and (**b**) changes in lattice constants of the perovskites as a function of EA or Br concentration.

The changes in the lattice constant attributed to the addition of EABr are shown in Figure 4b. The constant decreased with increasing EABr addition because Br had a smaller ionic radius than that of I. The slope of the lattice reduction was less than that for MAPbBr$_3$ (full substitution of Br) [8], which indicated that EA, which had a larger ionic radius than that of MA, also substituted at the MA site.

From the crystal orientation results, schematic models of randomly and (100)-oriented perovskite grains were developed and are depicted in Figure 5a,b, respectively. The grains in the standard device were randomly oriented, whereas the device with 30% added EABr had highly (100)-aligned crystals. The current value increased when EABr increased by 10% to 30%, which is due to a higher (100) orientation of the perovskite crystal. Large-angle grain boundaries that cause high electrical resistance are reduced by the addition of EA, as illustrated in Figure 5b, which leads to an increase in the current density, as observed in Figure 4a. The diffusion coefficient is inversely proportional to ionic radius, and the ionic radius of EA was larger than that of the MA, which decreases the diffusion coefficient and promotes slow and large crystal growth with a high (100) orientation.
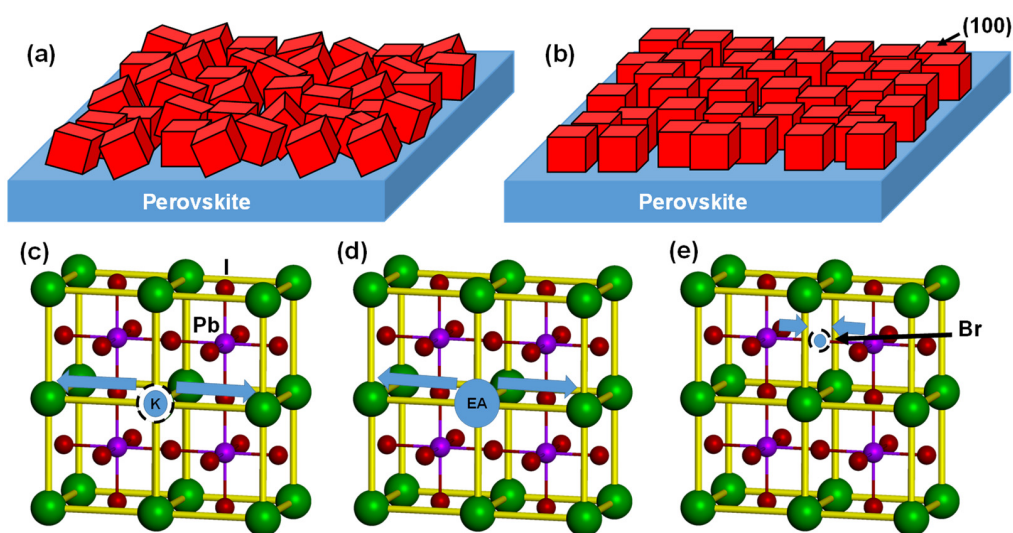

Figure 5. Schematic models of (**a**) randomly and (**b**) (100)-oriented perovskite grains. Changes in perovskite lattice due to the introduction of (**c**) K, (**d**) EA, and (**e**) Br.

Structure models of lattice constant changes induced by adding K, EA, or Br are shown in Figure 5c–e, respectively. As shown in Figure 5c, the K doping caused lattice expansion because of the inclusion of K in the MA defect [15]. A decrease in the current density of KI-added devices occurs because excess K can act as leakage current paths. The addition of the larger EA ionic radius also expanded the perovskite lattice (Figure 5d). In contrast, the small ionic radius of Br relative to that of I compressed the lattice, as shown in Figure 5e.

Band structures and the partial density of states of the MAPbI$_3$ and MA$_{0.625}$EA$_{0.25}$K$_{0.125}$PbI$_{2.5}$Br$_{0.5}$ perovskite crystals were calculated from the first-principles calculations [38–42]. The ab initio quantum calculations used the Vanderbilt ultra-soft pseudo-potentials, scalar relativistic generalized gradient approximations, and the Perdew–Burke–Ernzerhof exchange–correlation function and density functional theory (DFT + U, U = 6.0 eV) without considering the spin–orbital coupling effect (Quantum Espresso software) [43–46]. The initial parameters used for the EA/K-added crystal were $2 \times 2 \times 2$ supercells, experimental lattice constants, the kinetic energy cutoff for the wave functions (25 Ry), and the charge density (225 Ry). The structure models and electron density distributions for the standard and MA$_{0.625}$EA$_{0.25}$K$_{0.125}$PbI$_{2.5}$Br$_{0.5}$ perovskite crystals are shown in Figure 6a,b, respectively. The standard system of MAPbI$_3$ was calculated with a $1 \times 1 \times 1$ single cell, as shown in Figure 6a, and no specific differences were observed for the electron densities near Pb and I. In contrast, for the EABr-K-added perovskite crystal in Figure 6b, the electron density was

higher in the vicinity of Br relative to that for I. In addition, an electron distribution was observed near EA, while it was low and delocalized around K.
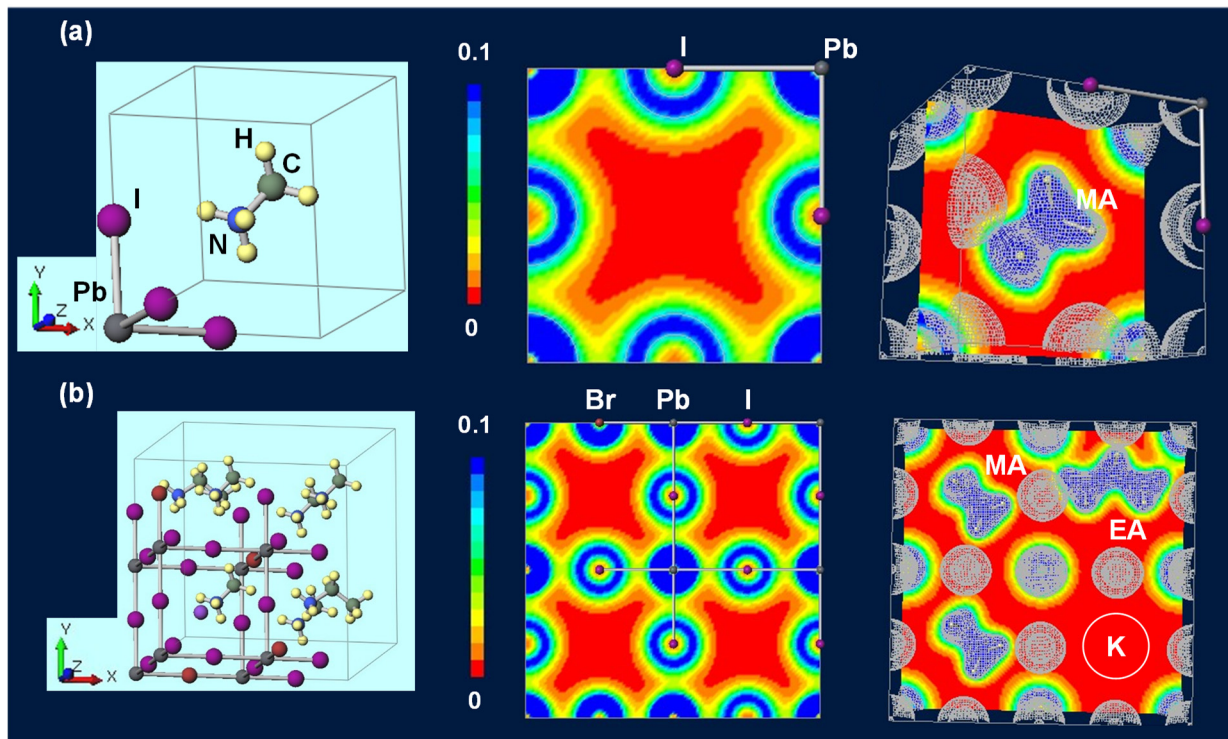

Figure 6. Crystal structures and calculated electron density distributions of (**a**) $MAPbI_3$ and (**b**) $MA_{0.625}EA_{0.25}K_{0.125}PbI_{2.5}Br_{0.5}$.

Figure 7a,b show the calculated band structures and density of states for $MAPbI_3$ and $MA_{0.625}EA_{0.25}K_{0.125}PbI_{2.5}Br_{0.5}$, respectively. The Fermi energy was set at zero. The density of states (DOS) and partial density of states (pDOS) were calculated to better understand the energy level for each orbital near the valence band and conduction band. The E_g values were calculated from the band structure, and Table 3 shows the E_g and total energies of the perovskite crystals. The E_g of $MAPbI_3$ and $MA_{0.625}EA_{0.25}K_{0.125}PbI_{2.5}Br_{0.5}$ was 1.340 eV and 1.377 eV, respectively, and E_g was larger for the $MA_{0.625}EA_{0.25}K_{0.125}PbI_{2.5}Br_{0.5}$ crystal relative to that for the standard $MAPbI_3$, which agreed with experimental results. The EA addition reduced the total energy and stabilized the perovskite crystal, which suppressed MA desorption. The density of states revealed that Br was dominant in the valence band of the $MA_{0.625}EA_{0.25}K_{0.125}PbI_{2.5}Br_{0.5}$ crystal, which improved the current density. The energy bandgap of $MAPbI_3$ was calculated to be 1.340 eV in the present work, which is smaller than the E_g of the well-known $MAPbI_3$ [47,48], which can be explained by two reasons. The first is a "bandgap problem [49,50]" of density functional theory [51,52], that is, too-small bandgaps have been calculated from the density functional theory. The second is related to the lattice constants. In a previous study [53], the bandgaps were calculated to be smaller when the smaller lattice constants were used. In the present work, lattice constants from the experimental data were used, which might be a little smaller in the calculation.

Table 3. Calculated energy gaps and difference of total energies.

Perovskite Crystal	E_g (eV)	Total Energy E (eV)	ΔE (eV cell^{-1})
$MAPbI_3$	1.340	−3504.0	0
$MA_{0.625}EA_{0.25}K_{0.125}PbI_{2.5}Br_{0.5}$	1.377	−3514.5	−10.5
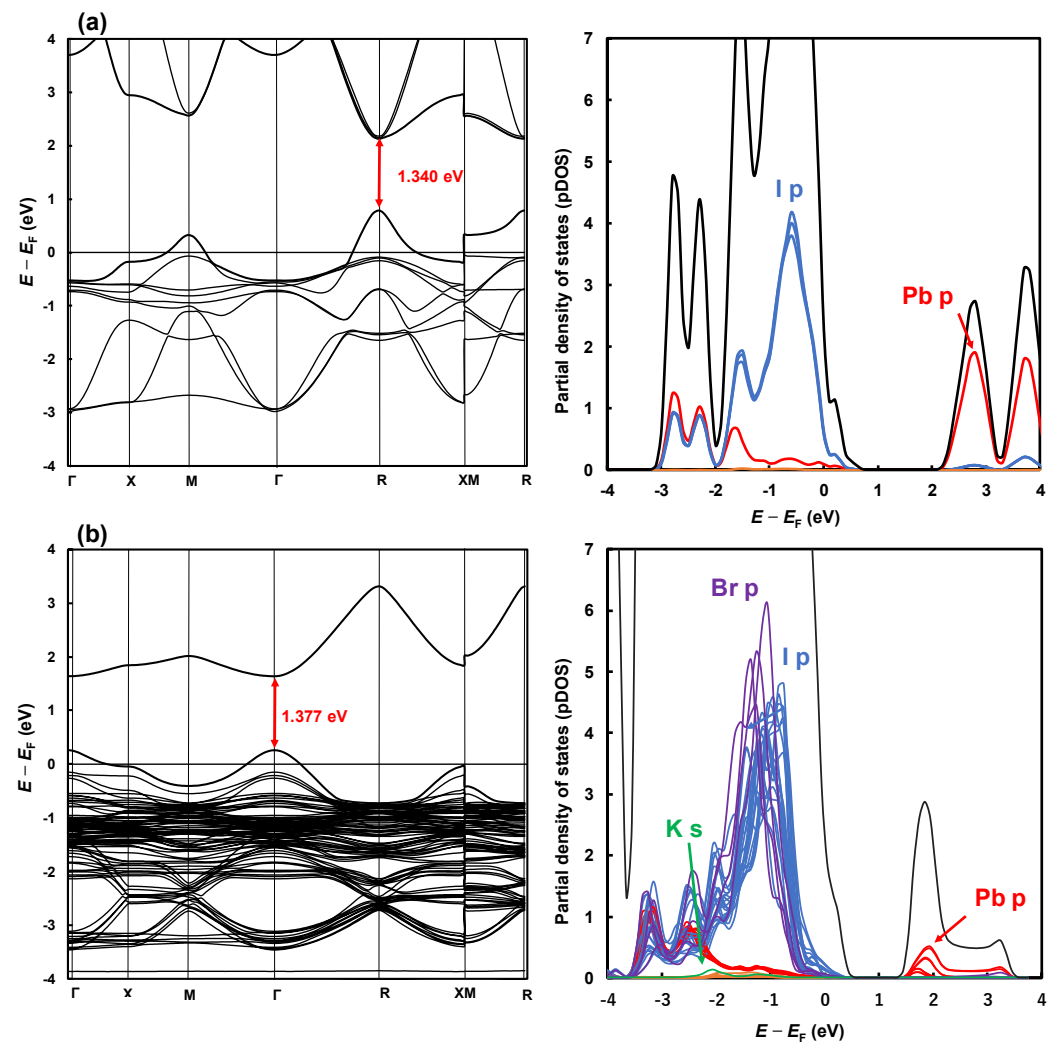
Figure 7. Band structures and density of states of (**a**) $MAPbI_3$ and (**b**) $MA_{0.625}EA_{0.25}K_{0.125}PbI_{2.5}Br_{0.5}$.

In the present work, DPPS was used on the perovskite layer. DPPS has two important features. First, the DPPS is stable at elevated temperatures above 300 °C, and the DPPS functions as a protective layer when deposited on perovskite compounds [28,29]. Second, polysilanes such as DPPS work as *p*-type semiconductors, which promote hole transfer [54]. Hence, DPPSs have been applied as hole transport layers [28,29] and as additives in the photoactive layer [55] of $MAPbI_3$ perovskite devices. The heat treatment at 190 °C in air conditions in the present study is very high compared to the well-known annealing conditions of 100 °C for $MAPbI_3$. As observed in the XRD patterns in Figure 3b, there were few degradations of $MAPbI_3$ during the annealing process. This is due to the excellent protection effect of the DPPS layer on the perovskite layer [29].

4. Conclusions

The effects of KI and EABr addition on the microstructures of the perovskite layers and the photovoltaic properties of $MAPbI_3$ photovoltaic devices were investigated. The *J-V* characteristics showed improvement in the device performance by introducing K and EA into the $MAPbI_3$ perovskite, and the device with the addition of KI 5% and EABr 30% exhibited the highest conversion efficiency of 12.88%. By using the air-blowing method and inserting a DPPS layer between the perovskite and spiro-OMeTAD layers, highly (100)-oriented cubic perovskite crystals were formed, which led to the increase in short-circuit current density. The addition of Br led to an increase in E_g, which resulted in the increase in the open-circuit voltage. First-principles calculations also showed the reduction in total

energy of the perovskite crystal by introducing EA, K, and Br, which agreed with the results of stabilities. The present work showed that co-addition of KI and EABr to the MAPbI$_3$ by using the air-blowing method and inserting a DPPS layer was an effective method for the fabrication of photovoltaic devices with improved properties.

Author Contributions: Conceptualization, S.T. and T.O.; methodology, S.T., T.O. and A.S.; formal analysis, S.T., T.O. and A.S.; investigation, S.T. and T.O.; resources, M.O., S.F., T.T. and T.H.; data curation, S.T. and T.O.; writing—original draft preparation, S.T. and T.O.; writing—review and editing, S.T., T.O., A.S., M.O., S.F., T.T. and T.H.; project administration, T.O.; funding acquisition, T.O. All authors have read and agreed to the published version of the manuscript.

Institutional Review Board Statement: Not applicable.

Informed Consent Statement: Not applicable.

Data Availability Statement: Data are contained within the article.

Conflicts of Interest: The authors declare no conflict of interest.

References

1. Kojima, A.; Teshima, K.; Shirai, Y.; Miyasaka, T. Organometal halide perovskites as visible-light sensitizers for photovoltaic cells. *J. Am. Chem. Soc.* **2019**, *131*, 6050–6051. [CrossRef] [PubMed]
2. Kim, H.-S.; Lee, C.-R.; Im, J.-H.; Lee, K.-B.; Moehl, T.; Marchioro, A.; Moon, S.-J.; Humphry-Baker, R.; Yum, J.-H.; Moser, J.E.; et al. Lead iodide perovskite sensitized all-solid-state submicron thin film mesoscopic solar cell with efficiency exceeding 9%. *Sci. Rep.* **2012**, *2*, 591. [CrossRef] [PubMed]
3. Lee, M.M.; Teuscher, J.; Miyasaka, T.; Murakami, T.N.; Snaith, H.J. Efficient hybrid solar cells based on meso-superstructured organometal halide perovskites. *Science* **2012**, *338*, 643–647. [CrossRef]
4. Burschka, J.; Pellet, N.; Moon, S.-J.; Humphry-Baker, R.; Gao, P.; Nazeeruddin, M.K.; Grätzel, M. Sequential deposition as a route to high-performance perovskite-sensitized solar cells. *Nature* **2013**, *499*, 316–320. [CrossRef] [PubMed]
5. Hu, Y.; Hutter, E.M.; Rieder, P.; Grill, I.; Hanisch, J.; Aygüler, M.F.; Hufnagel, A.G.; Handloser, M.; Bein, T.; Hartschuh, A.; et al. Understanding the role of cesium and rubidium additives in perovskite solar cells: Trap states, charge transport, and recombination. *Adv. Energy Mater.* **2018**, *8*, 1703057. [CrossRef]
6. Tyrren-Cruz, S.H.; Saliba, M.; Mayer, T.M.; Juarez-Santiesteban, H.; Mathew, X.; Nienhaus, L.; Tress, W.; Erodici, P.M.; Sher, M.-J.; Bawendi, G.M.; et al. Enhanced charge carrier mobility and lifetime suppress hysteresis and improve efficiency in planar perovskite solar cells. *Energy Environ. Sci.* **2018**, *11*, 78–86. [CrossRef]
7. Tailor, N.K.; Abdi-Jalebi, M.; Gupta, V.; Hu, H.; Dar, M.I.; Li, G.; Satapathi, S. Recent progress in morphology optimization in perovskite solar cell. *J. Mater. Chem. A* **2020**, *8*, 21356–21386. [CrossRef]
8. Oku, T. Crystal structures of perovskite halide compounds used for solar cells. *Rev. Adv. Mater. Sci.* **2020**, *59*, 264–305. [CrossRef]
9. Rao, M.K.; Sangeetha, D.N.; Selvakumar, M.; Sudhakar, Y.N.; Mahesha, M.G. Review on persistent challenges of perovskite solar cells' stability. *Sol. Energy* **2021**, *218*, 469–491. [CrossRef]
10. Oku, T.; Kandori, S.; Taguchi, M.; Suzuki, A.; Okita, M.; Minami, S.; Fukunishi, S.; Tachikawa, T. Polysilane-inserted methylammonium lead iodide perovskite solar cells doped with formamidinium and potassium. *Energies* **2020**, *13*, 4776. [CrossRef]
11. Zaccaria, F.; Zhang, B.; Goldoni, L.; Imran, M.; Zito, J.; van Beek, B.; Lauciello, S.; De Trizio, L.; Manna, L.; Infante, I. The reactivity of CsPbBr$_3$ nanocrystals toward acid/base ligands. *ACS Nano* **2022**, *16*, 1444–1455. [CrossRef] [PubMed]
12. Liu, C.; Kong, W.; Li, W.; Chen, H.; Li, D.; Wang, W.; Xu, B.; Cheng, C.; Jen, A.K.Y. Enhanced stability and photovoltage for inverted perovskite solar cells via precursor engineering. *J. Mater. Chem. A* **2019**, *26*, 15880–15886. [CrossRef]
13. Zhang, M.; Yun, J.S.; Ma, Q.; Zheng, J.; Lau, C.F.J.; Deng, X.; Kim, J.; Kim, D.; Seidel, J.; Green, M.A.; et al. High-efficiency rubidium-incorporated perovskite solar cells by gas quenching. *ACS Energy Lett.* **2017**, *2*, 438–444. [CrossRef]
14. Takada, K.; Oku, T.; Suzuki, A.; Okita, M.; Fukunishi, S.; Tachikawa, T.; Hasegawa, T. Fabrication and characterization of ethylammonium- and rubidium-added perovskite solar cells. *Chem. Proc.* **2022**, *9*, 14. [CrossRef]
15. Tang, Z.; Bessho, T.; Awai, F.; Kinoshita, T.; Maitani, M.M.; Jono, R.; Murakami, T.N.; Wang, H.; Kubo, T.; Uchida, S.; et al. Hysteresis-free perovskite solar cells made of potassium-doped organometal halide perovskite. *Sci. Rep.* **2017**, *7*, 12183. [CrossRef]
16. Zhao, W.; Yao, Z.; Yu, F.; Yang, D.; Liu, S. Alkali metal doping for improved CH$_3$NH$_3$PbI$_3$ perovskite solar cells. *Adv. Sci.* **2018**, *5*, 1700131. [CrossRef]
17. Abdi-Jalebi, M.; Andaji-Garmaroudi, Z.; Cacovich, S.; Stavrakas, C.; Philippe, B.; Richter, J.M.; Alsari, M.; Booker, E.P.; Hutter, E.M.; Pearson, A.J.; et al. Maximizing and stabilizing luminescence from halide perovskites with potassium passivation. *Nature* **2018**, *555*, 497–501. [CrossRef]

18.　Machiba, H.; Oku, T.; Kishimoto, T.; Ueoka, N.; Suzuki, A. Fabrication and evaluation of K-doped $MA_{0.8}FA_{0.1}K_{0.1}PbI_3(Cl)$ perovskite solar cells. *Chem. Phys. Lett.* **2019**, *730*, 117–123. [CrossRef]

19.　Yang, Y.; Wu, L.; Hao, X.; Tang, Z.; Lai, H.; Zhang, J.; Wanga, W.; Feng, L. Beneficial effects of potassium iodide incorporation on grain boundaries and interfaces of perovskite solar cells. *RSC Adv.* **2019**, *9*, 28561–28568. [CrossRef]

20.　Kandori, S.; Oku, T.; Nishi, K.; Kishimoto, T.; Ueoka, N.; Suzuki, A. Fabrication and characterization of potassium- and formamidinium-added perovskite solar cells. *J. Ceram. Soc. Jpn.* **2020**, *128*, 805–811. [CrossRef]

21.　Hsu, H.-L.; Chang, C.-C.; Chen, C.-P.; Jiang, B.-H.; Jeng, R.-J.; Cheng, C.-H. High-performance and high-durability perovskite photovoltaic devices prepared using ethylammonium iodide as an additive. *J. Mater. Chem. A* **2015**, *3*, 9271–9277. [CrossRef]

22.　Nishi, K.; Oku, T.; Kishimoto, T.; Ueoka, N.; Suzuki, A. Photovoltaic Characteristics of $CH_3NH_3PbI_3$ Perovskite Solar Cells Added with Ethylammonium Bromide and Formamidinium Iodide. *Coatings* **2020**, *10*, 410. [CrossRef]

23.　Oku, T.; Zushi, M.; Imanishi, Y.; Suzuki, A.; Suzuki, K. Microstructures and photovoltaic properties of perovskite-type $CH_3NH_3PbI_3$ compounds. *Appl. Phys. Express* **2014**, *7*, 121601. [CrossRef]

24.　Oku, T.; Ohishi, Y. Effects of annealing on $CH_3NH_3PbI_3$ (Cl) perovskite photovoltaic devices. *J. Ceram. Soc. Jpn.* **2018**, *126*, 56–60. [CrossRef]

25.　Ueoka, N.; Oku, T. Stability Characterization of PbI_2-added $CH_3NH_3PbI_{3-x}Cl_x$ photovoltaic devices. *ACS Appl. Mater. Interfaces* **2018**, *10*, 44443–44451. [CrossRef]

26.　Ueoka, N.; Oku, T. Effects of co-addition of sodium chloride and copper (ii) bromide to mixed-cation mixed-halide perovskite photovoltaic devices. *ACS Appl. Energy Mater.* **2020**, *9*, 7272–7283. [CrossRef]

27.　Oku, T.; Ohishi, Y.; Ueoka, N. Highly (100) -oriented $CH_3NH_3PbI_3$ (Cl) perovskite solar cells prepared with NH_4Cl using an air blow method. *RSC Adv.* **2018**, *8*, 10389–10395. [CrossRef]

28.　Taguchi, M.; Suzuki, A.; Oku, T.; Ueoka, N.; Minami, S.; Okita, M. Effects of annealing temperature on decaphenylcyclopentasilane-inserted $CH_3NH_3PbI_3$ perovskite solar cells. *Chem. Phys. Lett.* **2019**, *737*, 136822. [CrossRef]

29.　Oku, T.; Taguchi, M.; Suzuki, A.; Kitagawa, K.; Asakawa, Y.; Yoshida, S.; Okita, M.; Minami, S.; Fukunishi, S.; Tachikawa, T. Effects of polysilane addition to chlorobenzene and high temperature annealing on $CH_3NH_3PbI_3$ perovskite photovoltaic devices. *Coatings* **2021**, *11*, 665. [CrossRef]

30.　Suzuki, A.; Taguchi, M.; Oku, T.; Okita, M.; Minami, S.; Fukunishi, S.; Tachikawa, T. Additive effects of methyl ammonium bromide or formamidinium bromide in methylammonium lead iodide perovskite solar cells using decaphenylcyclopentasilane. *J. Mater. Sci. Mater. Electron.* **2021**, *32*, 26449–26464. [CrossRef]

31.　Mizuno, S.; Oku, T.; Suzuki, A.; Okita, M.; Fukunishi, S.; Tachikawa, T.; Hasegawa, T. Photovoltaic properties and microstructures of polysilane-added perovskite solar cells. *Chem. Proc.* **2022**, *9*, 20. [CrossRef]

32.　Oku, T.; Ueoka, N.; Suzuki, K.; Suzuki, A.; Yamada, M.; Sakamoto, H.; Minami, S.; Fukunishi, S.; Kohno, K.; Miyauchi, S. Fabrication and characterization of perovskite photovoltaic devices with TiO_2 nanoparticle layers. *AIP Conf. Proc.* **2017**, *1807*, 020014. [CrossRef]

33.　Ueoka, N.; Oku, T.; Tanaka, H.; Suzuki, A.; Sakamoto, H.; Yamada, M.; Minami, S.; Miyauchi, S.; Tsukada, S. Effects of PbI_2 addition and TiO_2 electron transport layers for perovskite solar cells. *Jpn. J. Appl. Phys.* **2018**, *57*, 08RE05. [CrossRef]

34.　Chen, H.-W.; Sakai, N.; Ikegami, M.; Miyasaka, T. Emergence of hysteresis and transient ferroelectric response in organo-lead halide perovskite solar cells. *J. Phys. Chem. Lett.* **2014**, *6*, 164–169. [CrossRef]

35.　Li, Z.; Yang, M.; Park, J.S.; Wei, S.H.; Berry, J.J.; Zhu, K. Perovskite structures by tuning tolerance factor: Formation of formamidinium and cesium lead iodide solid-state alloys. *Chem. Mater.* **2016**, *28*, 284–292. [CrossRef]

36.　Tanaka, H.; Oku, T.; Ueoka, N. Structural stabilities of organic-inorganic perovskite crystals. *Jpn. J. Appl. Phys.* **2018**, *57*, 08RE12. [CrossRef]

37.　Ferdowsi, P.; Ochoa-Martinez, E.; Alonso, S.S.; Steiner, U.; Saliba, M. Ultrathin polymeric films for interfacial passivation in wide band-gap perovskite solar cells. *Sci. Rep.* **2020**, *10*, 22260. [CrossRef]

38.　Ueoka, N.; Oku, T.; Suzuki, A. Effects of doping with Na, K, Rb, and formamidinium cations on $(CH_3NH_3)_{0.99}Rb_{0.01}Pb_{0.99}Cu_{0.01}I_{3-x}(Cl, Br)_x$ perovskite photovoltaic cells. *AIP Adv.* **2020**, *10*, 125023. [CrossRef]

39.　Suzuki, A.; Kitagawa, K.; Oku, T.; Okita, M.; Fukunishi, S.; Tachikawa, T. Additive effects of copper and alkali metal halides into methylammonium lead iodide perovskite solar cells. *Electron. Mater. Lett.* **2022**, *18*, 176–186. [CrossRef]

40.　Ono, I.; Oku, T.; Suzuki, A.; Okita, M.; Fukunishi, S.; Tachikawa, T.; Hasegawa, T. Effects of guanidinium addition to $CH_3NH_3PbI_3$ perovskite solar cells inserted with decaphenylpentasilane. *Chem. Proc.* **2022**, *9*, 13. [CrossRef]

41.　Suzuki, A.; Kishimoto, K.; Oku, T.; Okita, M.; Fukunishi, S.; Tachikawa, T. Additive effect of lanthanide compounds into perovskite layer on photovoltaic properties and electronic structures. *Synth. Met.* **2022**, *287*, 117092. [CrossRef]

42.　Enomoto, A.; Suzuki, A.; Oku, T.; Okita, M.; Fukunishi, S.; Tachikawa, T.; Hasegawa, T. Effects of Cu, K and guanidinium addition to $CH_3NH_3PbI_3$ perovskite solar cells. *J. Electron. Mater.* **2022**, *51*, 4317–4328. [CrossRef]

43.　Suzuki, A.; Oku, T. Effects of mixed-valence states of Eu-doped $FAPbI_3$ perovskite crystals studied by first-principles calculation. *Mater. Adv.* **2021**, *2*, 2609–2616. [CrossRef]

44.　Kishimoto, T.; Oku, T.; Suzuki, A.; Ueoka, N. Additive effects of guanidinium iodide on $CH_3NH_3PbI_3$ perovskite solar cells. *Phys. Status Solidi A* **2021**, *218*, 2100396. [CrossRef]

45.　Okumura, R.; Oku, T.; Suzuki, A.; Okita, M.; Fukunishi, S.; Tachikawa, T.; Hasegawa, T. Effects of adding alkali metals and organic cations to Cu-based perovskite solar cells. *Appl. Sci.* **2022**, *12*, 1710. [CrossRef]

46.　Ono, I.; Oku, T.; Suzuki, A.; Asakawa, Y.; Terada, S.; Okita, M.; Fukunishi, S.; Tachikawa, T. Fabrication and characterization of CH$_3$NH$_3$PbI$_3$ solar cells with added guanidinium and inserted with decaphenylpentasilane. *Jpn. J. Appl. Phys.* **2022**, *61*, SB1024. [CrossRef]

47.　Hayase, S. Research following pb perovskite solar cells. *Electrochemistry* **2017**, *85*, 222–225. [CrossRef]

48.　Jeyakumar, R.; Bag, A.; Nekovei, R.; Radhakrishnan, R. Interface studies by simulation on methylammonium lead iodide based planar perovskite solar cells for high efficiency. *Sol. Energy* **2019**, *190*, 104–111. [CrossRef]

49.　Ku, W.; Eguiluz, A.G. Band-gap problem in semiconductors revisited: Effects of core states and many-body self-consistency. *Phys. Rev. Lett.* **2002**, *89*, 126401. [CrossRef]

50.　Tan, H.; Liu, H.; Li, Y.; Duan, W.; Zhang, S. Understanding the origin of bandgap problem in transition and post-transition metal oxides. *J. Chem. Phys.* **2019**, *151*, 124703. [CrossRef]

51.　Kohn, W.; Sham, L.J. Self-consistent equations including exchange and correlation effects. *Phys. Rev.* **1965**, *140*, A1133–A1138. [CrossRef]

52.　Kohn, W. Nobel Lecture: Electronic structure of matter—Wave functions and density functionals. *Rev. Mod. Phys.* **1999**, *71*, 1253–1266. [CrossRef]

53.　Ong, K.P.; Wu, S.; Nguyen, T.H.; Singh, D.J.; Fan, Z.; Sullivan, M.B.; Dang, C. Multi band gap electronic structure in CH$_3$NH$_3$PbI$_3$. *Sci. Rep.* **2019**, *9*, 2144. [CrossRef]

54.　Oku, T.; Nakagawa, J.; Iwase, M.; Kawashima, A.; Yoshida, K.; Suzuki, A.; Akiyama, T.; Tokumitsu, K.; Yamada, M.; Nakamura, M. Microstructures and photovoltaic properties of polysilane-based solar cells. *Jpn. J. Appl. Phys.* **2013**, *52*, 04CR07. [CrossRef]

55.　Oku, T.; Nomura, J.; Suzuki, A.; Tanaka, H.; Fukunishi, S.; Minami, S.; Tsukada, S. Fabrication and characterization of CH$_3$NH$_3$PbI$_3$ perovskite solar cells added with polysilanes. *Int. J. Photoenergy* **2018**, *2018*, 8654963. [CrossRef]